Improved electrochemical performance of rare earth doped LiMn$_{1.5-x}$Ni$_{0.5}$RE$_x$O$_4$ based cathodes for lithium-ion batteries

Pura Ram[1], A. Gören[2,3], R. Gonçalves[2,3], Ganpat Choudhary[1], S. Ferdov[2], M. M. Silva[3], Rahul Singhal[4], C. M. Costa[2,3*], Rakesh K. Sharma[1*], S. Lanceros-Méndez[2,5,6]

[1]Department of Chemistry, Indian Institute of Technology Jodhpur, 342011, Rajasthan, India

[2]Centre of Physics, University of Minho, 4710-057 Braga, Portugal

[3]Centre/Department of Chemistry, University of Minho, 4710-057 Braga, Portugal

[4]Department of Physics and Engineering Physics, Central Connecticut State University, New Britain, CT, 06067, USA

[5]BCMaterials, Parque Científico y Tecnológico de Bizkaia, 48160 Derio, Spain

[6]IKERBASQUE, Basque Foundation for Science, 48013 Bilbao, Spain

Abstract

LiMn$_{1.5}$Ni$_{0.5}$O$_4$ with spinel type of structure was synthesized by sol-gel method and doped by different rare-earth elements (Nd, Gd and Dy). It was found that the inclusion of rare-earth element preserves the cubic spinel structure, leads to smaller particle size and improves the cyclic performance of the produced batteries. The best battery performance was obtained after doping the spinel structure by Gd. Among the used rare-earth elements Gd is the only one with stable oxidation state of 3+ which leads to stabilization of the Mn dissolution.

Thus, the improvements observed in battery performance (rate performance and cycle life) are due to the superior structural stability of the doped active materials. It is concluded that the LiMn$_{1.48}$Ni$_{0.5}$Gd$_{0.02}$O$_4$ sample is the one with the best overall performance to act as active material for cathodes in rechargeable lithium-ion batteries.

Keywords: LiMn$_{1.5}$Ni$_{0.5}$O$_4$, rare earth, cathodes, lithium-ion batteries

1. Introduction

Environmental issues with respect to global warming and the necessary reduction of CO_2 emission exerts great pressure for the development of efficient electrical energy storage systems to support the use of energy generated by environmental friendly sources, such as photovoltaic, wind and geothermal [1, 2]. The main energetic challenge is developing efficient energy storage systems, i.e, batteries, for electric vehicles (EV) and hybrid electric vehicles (HEV), leading to a strong reduction of CO_2 emissions and fossil fuel consumption [3, 4].

Batteries are the most used energy storage systems due to the larger amounts of energy stored in comparison to related systems, i.e, fuel cells and supercapacitors. The battery type most widely used is the lithium-ion battery, with a market share of 75% [5, 6].

The main components of a lithium-ion battery are the anode, cathode and separator/electrolyte [7]. Each constituent has specific function in the operation of the battery: the cathode (positive electrode) is responsible for the cell capacity and cycle life; the anode (negative electrode) should have a low potential in order to provide a high cell voltage with the cathode [8]; the separator is placed between electrodes and allows to control the movement and number of the ions between anode and cathode during charge and discharge and prevents the short-circuit of the battery [9]. Independently the type of cathode, they are typically composed by a polymer binder, conductive additive and the corresponding active material. In this structure, the polymer binder has the role of binding the active material and conductive additive, the conductive additive increases the electrical conductivity of the cathode and the active material acts as lithium reservoir in the electrode [10].

The active material used for cathode development must be easily reducible; react with lithium in a reversible way; be a good electronic conductor and stable. Few examples of

cathode materials for Li ion rechargeable batteries are $LiCoO_2$ [11], [Li, Mn, Ni, Co]O_2 [12], lithium metal polyoxyanion $Li_3V_2PO_4$ [13], $LiMn_{1.5}Ni_{0.5}O_4$ [14], $LiMPO_4$ and $LiMSiO_4$ (M=Mn, Fe, Co, and combinations of them) [15].

The manganese spinel cathode $LiMn_2O_4$ has been used in the first generation of plug-in hybrid electric vehicles or electric vehicles due to the high operating voltage above 4.0 V. Despite that, this spinel cathode shows high manganese solubility in the electrolyte, associated with a high concentration of Mn^{3+} ions, and a high capacity fading [16-18].

The operating voltage depends on the material type and in case of $LiFePO_4$, $LiCoO_2$ and $LiMn_{1.5}Ni_{0.5}O_4$ it is 3.4 V, 3.9 V and 4.7 V, respectively, the higher voltage of $LiMn_{1.5}Ni_{0.5}O_4$ is related to the Ni^{4+}–Ni^{2+} couple, the Mn^{4+} ions acting as inactive ions and reducing manganese solubility [4].

The spinel cathode $LiMn_{1.5}Ni_{0.5}O_4$ has received great interest due to its advantages as high operating voltage of ~ 4.7 V, high energy density of 650 $Wh.kg^{-1}$ and theoretical capacity of 146.7 $mAh.g^{-1}$ [19, 20]. Through the addition of the Ni element, $LiMn_{1.5}Ni_{0.5}O_4$ avoids the Jahn-Teller (JT) distortion of $LiMn_2O_4$ and can crystallize in two structures: a simple cubic phase denominated by "ordered spinel" (*P4332*) in which Li, Ni and Mn, atoms occupy the 8c, 4a and 12d sites, respectively, whereas the O(1) and O(2) oxygen atoms occupy in the 24e and 8c sites, and a face-centered cubic phase denominated by "disordered spinel" (*Fd3m*) where Ni and Mn atoms are randomly distributed in the 16d sites, whereas Li and O occupy 8a tetrahedral sites and 32e sites, respectively [20-24].

Cathodes based on this spinel structure show capacity fade resulting from an aggressive side reaction with the electrolyte that occurs at high-voltage operation [14]. One strategy for reducing this issue is the substitution of nickel and/or manganese and/or oxygen in the structure by small amounts of different atoms (cations and anions) that also improve the

electronic and ionic conductivity of this spinel structure [14, 20]. The different atoms that have been used for doping this spinel structure include Al, Co, Cr, Cu, F, Fe, Ga, Mg, Mo, Nb, Rh, Ru, S, Sm, Ti, V, W and Zn [19, 25-41]. Typically, the doping of $LiMn_{1.5}Ni_{0.5}O_4$ leads to improved cyclic performance and rate capability of the battery [14].

For $LiMn_{1.5}Ni_{0.5}O_4$, atoms with valence (+3) induce a charge compensation from a corresponding amount of manganese, giving rise to mixed Mn^{3+} and Mn^{4+} ions in the lattice, which improve rate capability. In this scope, the goal of this work is the synthesis, characterization and battery performance evaluation of $LiMn_{1.5}Ni_{0.5}O_4$ doped with different rare earth elements (REE), i.e, neodymium (Nd), Gadolinium (Gd), classified as light REE, and Dysprosium (Dy), classified as heavy REE, in order to evaluate the effects of both rare-earth element and quantity, the latter being performed for Gd. Further, the REE used in this work are the most used in many applications, including lasers and magnets, among others.

2. Experimental

2.1. Synthesis of the active materials

$LiMn_{1.5}Ni_{0.5}O_4$, $LiMn_{1.48}Gd_{0.02}Ni_{0.5}O_4$ and $LiMn_{1.5-x}Ni_{0.5}RE_xO_4$ (RE: Gd, Nd, Dy; x=0.04) were synthesized via sol gel route with analytical grade chemicals. Stoichiometric mixtures of lithium acetate, manganese acetate, nickel acetate, gadolinium acetate, neodymium acetate and dysprosium acetate were obtained in stoichiometry ratio from Alfa Aesar, USA. The raw powders were subjected to heating treatment to reach phase purity and stable form of the materials. Each constituent was dissolved in 2-ethylhexanoic acid to get a homogeneous solution at a temperature 100-150 ºC for 10-30 minutes and at a magnetic stirring rate of 250 rpm. After completely dissolution of each component, these were added into manganese acetate solution. More details of the synthesis process are described in [16]. The brownish precursors of the synthesized spinel undergo a two-step heat treatment. The removal of organic impurities and phase purity were obtained at 450 ºC for 4 hours and at 850 ºC for 14 hours in a box furnace, Nabertherm GmbH, Germany. The phase pure powder was ball milled for 6 hours with 10:1 ball weight/ material weight ratio in a planetary high energy ball milling, Retsch (PM-100 model).

2.2. Powder characterization

The surface morphology and elemental analysis of the samples were studied by Scanning Electron Microscopy (SEM) using Carl Zeiss, Evo special addition. The beam current

during surface morphology and energy dispersive X-ray were 80 pA and 200 nA respectively.

High resolution transmission electron microscopy (HRTEM) measurements were performed with a TEM Tecnai G2 instrument by FEI with an accelerating voltage of 200 kV. The physical characterization of pure phase powders was carried out using X-ray diffractogram, Brucker D8 advance, in the range two theta angle 10°- 80° with 0.02° per second scan rate in locked coupled mode. The amounts of the as-synthesized phases were determined by the method of Rietveld using TOPAS-3 software (Bruker AXS Inc.). The method involved fit the complete experimental diffraction patterns with calculated profiles and backgrounds. The phases included in the quantification were identified by the EVA software (EVA Software, DIFFRACplus Release 2006, Bruker AXS). Raman analysis were performed with 2 mW power air cooled LASER excitation source (operating at 532 nm) using an STR 500, Airix Japan, spectrophotometer. BET surface analysis was performed in AutoSorb(iQ3), Quantunchrome Instrument, USA. Experiments were carried out in 300 mg samples that were degassed in H_2 atmosphere pressure at 300 ℃ for 2 hr and the 20 points adsorption and desorption were measured in N_2 atmosphere.

2.3. Cathode preparation and half-cell fabrication

The cathode slurry was prepared with $LiMn_{1.5}Ni_{0.5}O_4$, $LiMn_{1.48}Gd_{0.02}Ni_{0.5}O_4$ and $LiMn_{1.5-x}Ni_{0.5}RE_xO_4$ (RE: Gd, Nd, Dy; x=0.04), carbon black and poly(vinylidene fluoride) (PVDF, Solvay 5130) in a 80:10:10 weight ratio (%), respectively, and N-methylpyrrolidone (NMP, Fluka). The PVDF was dissolved in NMP to form the binder solution and the other components (active material and conductive additive) were dried mixed. Then, small amounts of solid material (active material and conductive additive)

were added to the PVDF binder solution under constant stirring. After adding all solid material, it was left stirring during 2 hours at 1000 rpm to obtain a good dispersion. The slurry was spread uniformly on Al metal grade foil and dried in a furnace at 80 °C for 2 hours. The prepared cathodes were dried overnight at 90 °C in vacuum. Li metal foil was used as anode material, Whatman glass microfiber filters (grade GF/A) used as separator and 1M $LiPF_6$ in ethylene carbonate + dimethyl carbonate (EC+DMC, 1:1) from Solvionic as electrolyte. Swagelok type-cells (two or three electrodes) were assembled in a home-made argon-filled glove box. Different electrochemical tests were performed with the cells. Galvanostatic cycling was carried out at different C rates (C/8, C/5, C/2, C and 2C) between a minimum and a maximum limit of 3.5 V and 4.9 V, respectively, using Landt CT2001A Instrument. Electrochemical impedance spectroscopy was measured with an Autolab PGSTAT12 instrument in a frequency range from 1 MHz to 10 mHz with an amplitude of 10 mV. The cyclic voltamogram (CV) was performed in the range from 3.5 V to 4.9 V at the scan rate 0.1 mV/sec.

3. Results and discussion

$LiMn_{1.5}Ni_{0.5}O_4$ particles doped with different rare earth (RE) elements – Gd, Nd and Dy ($LiMn_{1.5-x}Ni_{0.5}RE_xO_4$; x = 0.02 and 0.04) were synthesized via sol gel. The effects of rare-earth doping element and concentration on the crystal structure and electrochemical performance were evaluated.

3.1. Synthesized powder properties

Figure 1 shows the surface morphology of the $LiMn_{1.5}Ni_{0.5}O_4$ powder obtained by SEM and detailed TEM images of the $LiMn_{1.5}Ni_{0.5}O_4$, $LiMn_{1.48}Ni_{0.5}Gd_{0.02}O_4$, $LiMn_{1.46}Ni_{0.5}Gd_{0.04}O_4$, $LiMn_{1.46}Ni_{0.5}Ny_{0.04}O_4$ and $LiMn_{1.46}Ni_{0.5}Dy_{0.04}O_4$ particles.
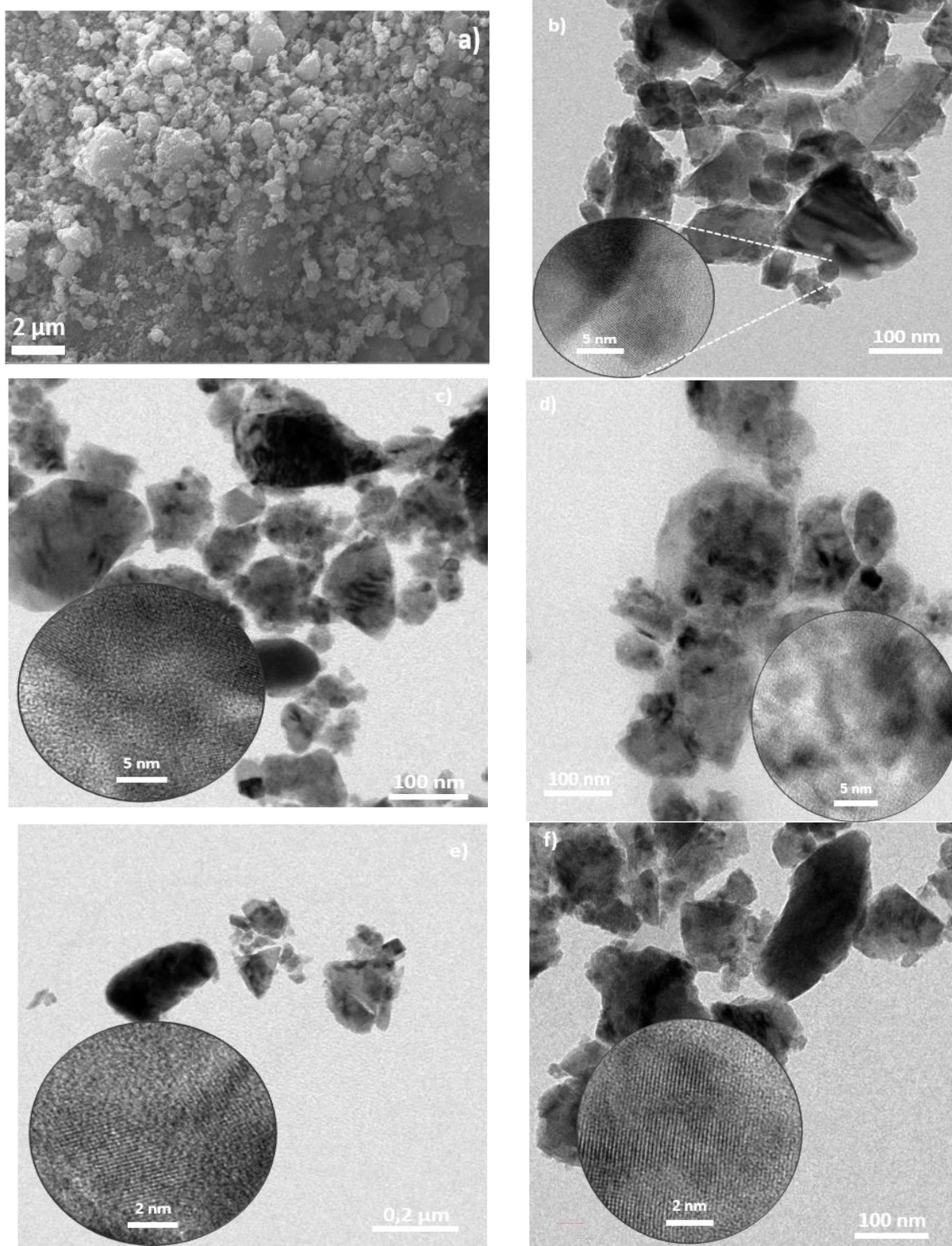
Figure 1 - SEM image of $LiMn_{1.5}Ni_{0.5}O_4$ (a) and TEM images of $LiMn_{1.5}Ni_{0.5}O_4$ (b), $LiMn_{1.48}Ni_{0.5}Gd_{0.02}O_4$ (c), $LiMn_{1.46}Ni_{0.5}Gd_{0.04}O_4$(d), $LiMn_{1.46}Ni_{0.5}Ny_{0.04}O_4$ (e) and $LiMn_{1.46}Ni_{0.5}Dy_{0.04}O_4$ (f) powders. Inset TEM images shows the atomic arrangement of the samples.

The SEM image of $LiMn_{1.5}Ni_{0.5}O_4$ (Figure 1a), also representative for the rest of the particles, reveals that the powder shows a non-homogenous size, which is confirmed by the TEM images, Figures 1b)-f), showing that the particle size ranges between 50 nm and 200 nm. The inserts of the Figures 1b)-f) show HRTEM. It should be mentioned that these images confirm the crystallinity of the particles.

The particle shape is not spherical, but in polyhedron form, in which the smaller polyhedron are assembles together to form large polyhedron secondary particles. Thus, the larger particle sizes are due to agglomeration.

The inset in Figure 1b) shows that the atomic arrangement for $LiMn_{1.5}Ni_{0.5}O_4$ is in a well-defined planar structure. Figure 1c-d) for $LiMn_{1.48}Ni_{0.5}Gd_{0.02}O_4$ and $LiMn_{1.46}Ni_{0.5}Gd_{0.04}O_4$ reveal a larger agglomeration trend when compared to the other samples, as evidenced by a dull planar structure. Figure 1e-f) for $LiMn_{1.5}Ni_{0.5}O_4$ doped with Nd and Dy shows less agglomerated and finer particle size when compared to the other samples. $LiMn_{1.46}Ni_{0.5}Dy_{0.04}O_4$ (Figure 1f) demonstrates a defined structure than the other samples, as confirmed by the clarity and contrast in planar structure.

The TEM images for all particles (Figure 1b-f) show the lattice fringes of the (111) plane of cubic spinel $LiMn_{1.5}Ni_{0.5}O_4$, revealing the high crystallinity present in the samples.

The selected area electron diffraction (SAED) patterns of $LiMn_{1.5}Ni_{0.5}O_4$ and $LiMn_{1.48}Ni_{0.5}Gd_{0.02}O_4$ show the inner and intense circle corresponding to the (111) plane and the next successive rings corresponding to (311) and (400), respectively (see supplementary information S1). The results are similar for the rest of the doped samples. The mapping of the elements was analyzed through SEM assisted EDX and it is shown in Figure 2 a)-c) for $LiMn_{1.5}Ni_{0.5}O_4$ powder and in figure 2d), $LiMn_{1.46}Dy_{0.04}Ni_{0.5}O_4$ powder. Figure 2d) for Dy is representative for other rare-earth element doping into $LiMn_{1.5}Ni_{0.5}O_4$ powder.

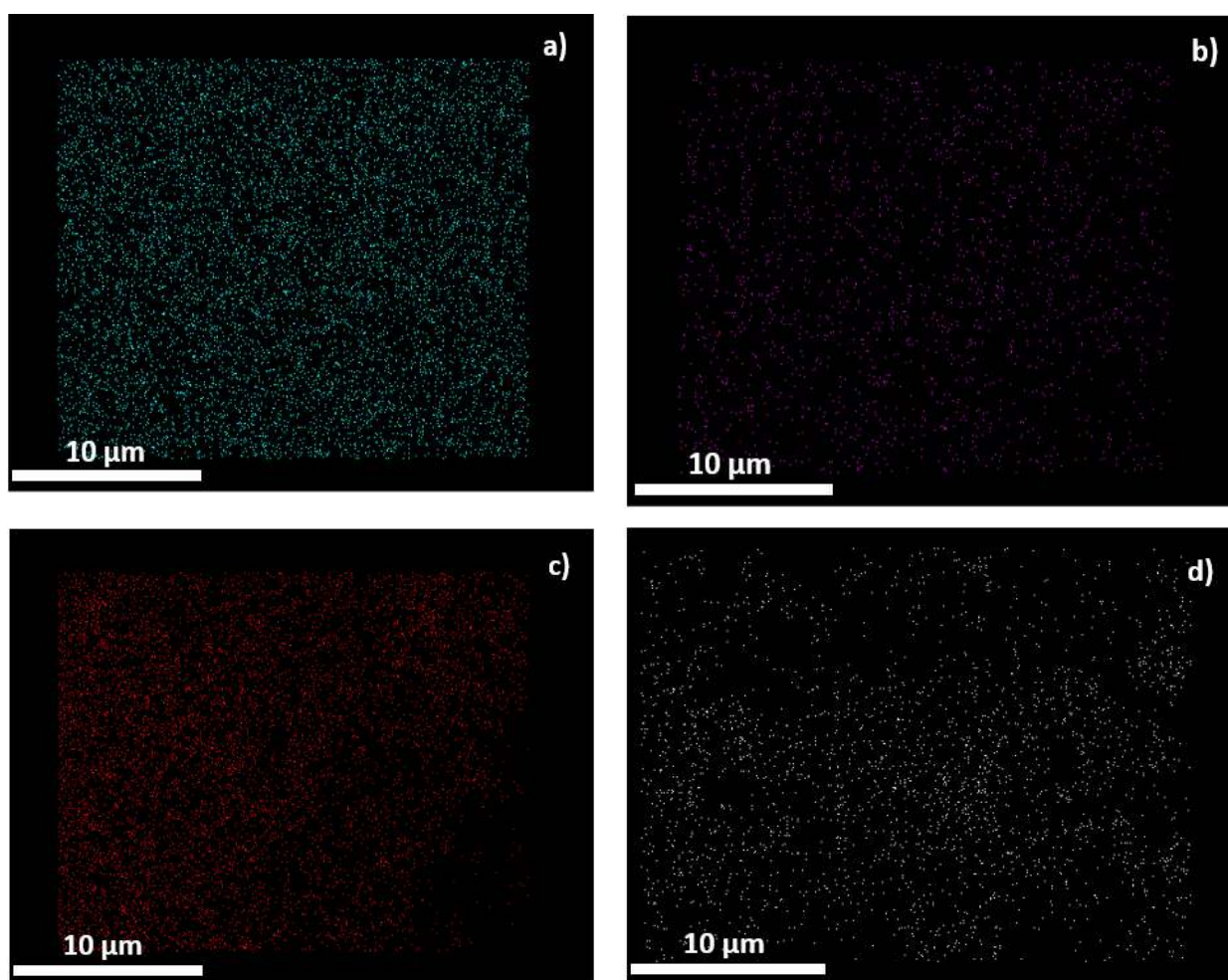**Figure 2** – EDX mapping for $LiMn_{1.5}Ni_{0.5}O_4$ powder: a) Mn element, b) Ni element and c) O element and d) Dy element into $LiMn_{1.46}Dy_{0.04}Ni_{0.5}O_4$ powder.

Figure 2 shows the uniform distribution of Mn, Ni and O through-out the nano-regime, the lower intensity of Ni element being due to the lower atomic concentration. Figure 2d) shows the rare-earth doping elemental mapping showing also homogeneous distribution Dy in the samples.

Table 1 shows slight differences in the chemical composition of each element (Mn, Ni, O and RE) for the different samples. Further, the elemental composition for the different samples is nearly in the stoichiometric ratio.

Table 1 – Elemental atomic composition obtained from SEM-EDX for $LiMn_{1.5}Ni_{0.5}O_4$, $LiMn_{1.48}Gd_{0.02}Ni_{0.5}O_4$ and $LiMn_{1.5-x}Ni_{0.5}RExO_4$ (RE: Gd, Nd, Dy; x=0.04)

Sample description	Elemental Atomic (%)			
	Mn	Ni	O	RE
$LiMn_{1.5}Ni_{0.5}O_4$	24.41	7.67	68.92	0.0
$LiMn_{1.48}Ni_{0.5}Gd_{0.02}O_4$	23.85	6.09	69.21	1.05
$LiMn_{1.46}Ni_{0.5}Gd_{0.04}O_4$	23.77	7.65	66.14	2.44
$LiMn_{1.46}Ni_{0.5}Nd_{0.04}O_4$	20.11	7.51	68.15	3.23
$LiMn_{1.46}Ni_{0.5}Dy_{0.04}O_4$	22.98	6.25	68.67	2.10

Figure 3 shows the X-ray diffraction patterns of $LiMn_{1.50}Ni_{0.5}O_4$, $LiMn_{1.48}Gd_{0.02}Ni_{0.5}O_4$, $LiMn_{1.46}Gd_{0.04}Ni_{0.5}O_4$, $LiMn_{1.46}Nd_{0.04}Ni_{0.5}O_4$ and $LiMn_{1.46}Dy_{0.04}Ni_{0.5}O_4$. All the patterns were successfully refined starting with model of cubic spinel phase and space group Fd3m (JCPDS card No. 35-782) [14, 20]. Small amounts of impurities (below 10%) were detected only in the $LiMn_{1.46}Nd_{0.04}Ni_{0.5}O_4$ and $LiMn_{1.46}Dy_{0.04}Ni_{0.5}O_4$ samples. The secondary phases were evaluated by Rietveld analysis and it was found the presence of Ni_6MnO_8, NiO, Mn_2O_3 and MnO_2 impurities indicated in the Figure 4 by arrows. These results are in agreement with previous literature in which the presence of impurities is ascribed to oxygen deficiency while keeping the spinel structure during the sintering process [37].
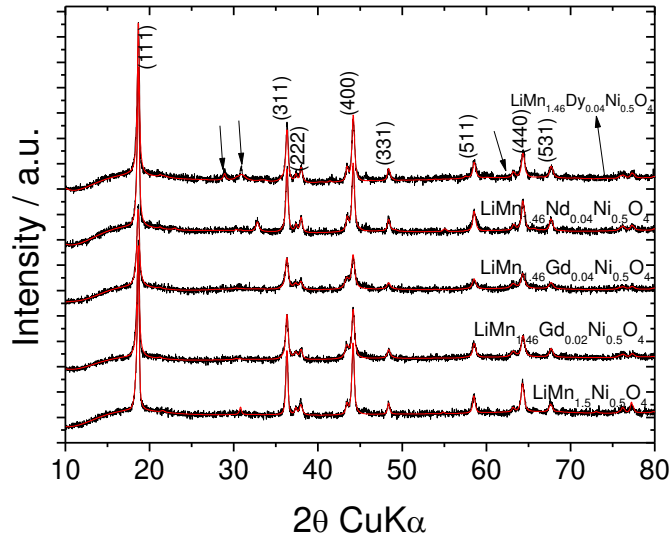
Figure 3 - Refined (red: calculated; black: experimental) XRD patterns for $LiMn_{1.5}Ni_{0.5}O_4$, $LiMn_{1.48}Gd_{0.02}Ni_{0.5}O_4$ and $LiMn_{1.5-x}Ni_{0.5}RExO_4$ (RE: Gd, Nd, Dy; x=0.04).

Table 2 presents the lattice parameters, full width at half maxima (FWHM) and the ratio of intensity of plane (311) to plane (400). The lattice constants for $LiMn_{1.50}Ni_{0.5}O_4$, $LiMn_{1.48}Gd_{0.02}Ni_{0.5}O_4$, $LiMn_{1.46}Gd_{0.04}Ni_{0.5}O_4$, $LiMn_{1.46}Nd_{0.04}Ni_{0.5}O_4$ and $LiMn_{1.46}Dy_{0.04}Ni_{0.5}O_4$ are 8.23, 8.24, 8.24, 8.24 and 8.24 Å respectively.

Table 2 - XRD structural parameters for $LiMn_{1.5}Ni_{0.5}O_4$, $LiMn_{1.48}Gd_{0.02}Ni_{0.5}O_4$ and $LiMn_{1.5-x}Ni_{0.5}RExO_4$ (RE: Gd, Nd, Dy; x=0.04).

Sample description	Lattice parameters /Å	Unit cell volume / Å³	FWHM / °	$I_{(400)}/I_{(311)}$
$LiMn_{1.5}Ni_{0.5}O_4$	8.23	556.9	0.29	1.25
$LiMn_{1.48}Ni_{0.5}Gd_{0.02}O_4$	8.24	560.4	0.35	1.14
$LiMn_{1.46}Ni_{0.5}Gd_{0.04}O_4$	8.24	560.4	0.41	1.11
$LiMn_{1.46}Ni_{0.5}Nd_{0.04}O_4$	8.24	558.7	0.28	1.10
$LiMn_{1.46}Ni_{0.5}Dy_{0.04}O_4$	8.24	558.7	0.30	1.28

The lattice constant slightly increases with rare-earth doping with respect to $LiMn_{1.50}Ni_{0.5}O_4$. These increases are attributed to the large ionic radius of rare earth elements Nd^{+3} (0.1 nm) > Gd^{+3} (0.0938 nm) > Dy^{3+} (0.0912 nm) compared to Mn^{3+} (0.064 nm) and Mn^{+4} (0.054 nm). Further, the changes in lattice parameter can be used as an indirect evidence for RE/Mn substitution [37].

The value of FWHM for all samples corresponding to the (111) plane peak was analyzed and it is found 0.287° for undoped $LiMn_{1.50}Ni_{0.5}O_4$ whereas it varies from 0.281° - 0.411° for $LiMn_{1.48}Gd_{0.02}Ni_{0.5}O_4$ and $LiMn_{1.5-x}Ni_{0.5}RE_xO_4$ (RE: Gd, Nd, Dy; x=0.04). The absence of impurity phases in $LiMn_{1.48}Gd_{0.02}Ni_{0.5}O_4$ and $LiMn_{1.46}Gd_{0.04}Ni_{0.5}O_4$ reveals that Gd^{+3} is able to replace the octahedral site element in place of the Mn^{+3}/Mn^{+4} site at 16d. To measure the occupancy of the octahedral site, the peak intensity ratio (400)/(311) was calculated and shown in table 2. The ratio decreases with Gd and Nd elemental doping whereas in the case of Dy the ratio almost match with undoped $LiMn_{1.50}Ni_{0.5}O_4$ which supports the octahedral site occupancy [42].

The Raman spectra recorded for all spinel doped and undoped samples show two major vibrational peaks at 625 cm^{-1} and 488 cm^{-1} characteristic of the Fd-3m phase (see supplementary information S2).

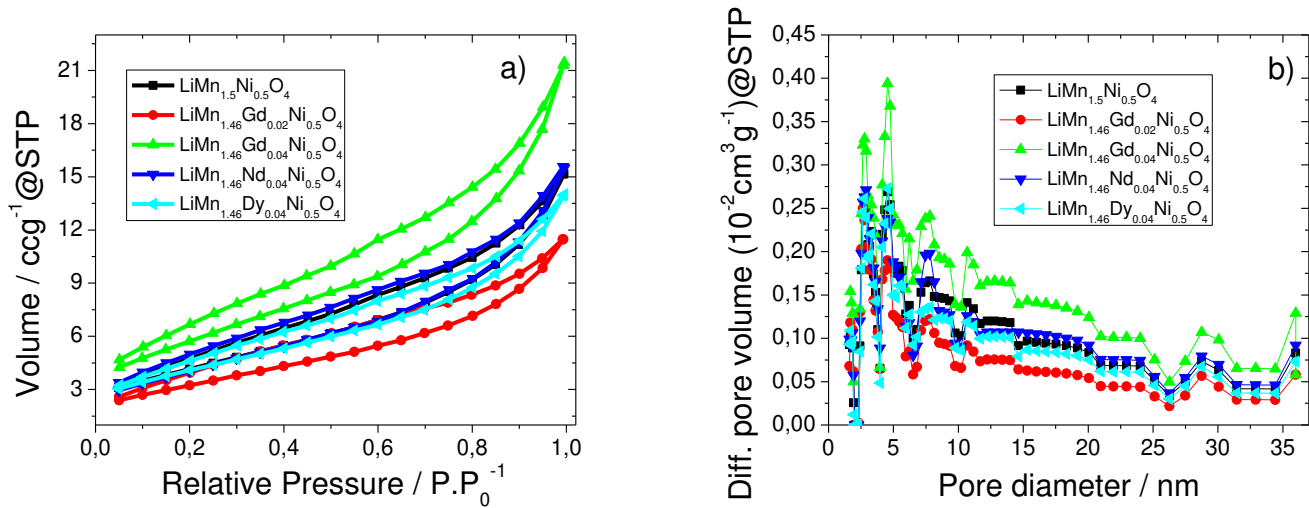The nitrogen adsorption-desorption isotherms and pore size distribution are shown in Figure 4.

Figure 4 - (a) N_2 adsorption - desorption isotherms and (b) pore size distribution for $LiMn_{1.5}Ni_{0.5}O_4$, $LiMn_{1.48}Gd_{0.02}Ni_{0.5}O_4$ and $LiMn_{1.5-x}Ni_{0.5}RExO_4$ (RE: Gd, Nd, Dy; x=0.04).

$LiMn_{1.5}Ni_{0.5}O_4$, $LiMn_{1.46}Nd_{0.04}Ni_{0.5}O_4$ and $LiMn_{1.46}Dy_{0.04}Ni_{0.5}O_4$ exhibit a meso-porous polyhedral crystal structure having 15 m^2/g specific surface area evaluated by multi point Brunauer-Emmett-Teller (BET) method as is observed in the Figure 4a) and also table 3.

Table 3 - BET parameters of $LiMn_{1.5}Ni_{0.5}O_4$, $LiMn_{1.48}Gd_{0.02}Ni_{0.5}O_4$ and $LiMn_{1.5-x}Ni_{0.5}RExO_4$ (RE: Gd, Nd, Dy; x=0.04).

	BET parameters	
Sample description	**Surface area / m^2/g**	**Average pore size / nm**
$LiMn_{1.5}Ni_{0.5}O_4$	15	3.1
$LiMn_{1.48}Ni_{0.5}Gd_{0.02}O_4$	12	3.0
$LiMn_{1.46}Ni_{0.5}Gd_{0.04}O_4$	21	3.2
$LiMn_{1.46}Ni_{0.5}Nd_{0.04}O_4$	15	3.2
$LiMn_{1.46}Ni_{0.5}Dy_{0.04}O_4$	15	3.0

However, the specific surface area for $LiMn_{1.46}Gd_{0.04}Ni_{0.5}O_4$ is 21 m^2/g whereas for $LiMn_{1.48}Gd_{0.02}Ni_{0.5}O_4$ is 12 m^2/g in which the increase of Gd content reduces the particle size, which can be attributed to an agglomeration process. The pore-size distribution, Figure 4b), reveals that the different materials show a wide range of pore sizes from 2 to 35 nm, with an average pore size of 3 nm. Thus, the samples have a non-homogeneous surface morphology.

3.2. Electrochemical properties

Cathodes were prepared from the active materials by previously synthesized by sol gel method and the electrochemical properties evaluated.

3.2.1. *Charge-discharge performance*

The charge-discharge profiles of $LiMn_{1.5}Ni_{0.5}O_4$ and $LiMn_{1.46}Gd_{0.04}Ni_{0.5}O_4$ for the 5th cycle at different scan rates and room temperature are shown in Figure 5a) and b), respectively. The shape of the charge-discharge curves for the others $LiMn_{1.5}Ni_{0.5}O_4$ doped powders are similar to the ones presented in Figure 5b, with variations in the charge and discharge value.

Independently of the samples, Figure 5 shows three voltage plateaus at ~ 4.0V, 4.6 V and 4.7 V corresponding to Mn^{3+}-Mn^{4+}, Ni^{2+}-Ni^{3+} and Ni^{3+}-Ni^{4+} redox processes, respectively [43]. These plateaus can be observed in details through of cyclic voltammetry results (Figure 8).

The plateaus at ~ 4.0V and 4.6 V- 4.7 V are attributed to lithium-ion insertion into 16c octahedral and 8a tetrahedral sites of the spinel structure, respectively.

From Figure 5a), the discharge capacity of $LiMn_{1.5}Ni_{0.5}O_4$ is 98.5, 101.7, 100.5, 89 and 32 mAh.g^{-1} at the rates of C/8, C/5, C/2, C and 2C, respectively, due to increased polarization at higher current rates.

The low value of the discharge capacity at C/8 is due to the formation of the solid electrolyte interface (SEI) layer, as at such a high voltage unwanted electrolyte occurs leaving decomposition products [44].

Figure 5a also shows for low scan rates (C/8) a large irreversible capacity, which is typically observed in the literature for this active material with conventional electrolytes [44].

For $LiMn_{1.46}Gd_{0.04}Ni_{0.5}O_4$ the discharge capacity is 62.5, 70.6, 75.8, 74.5 and 65.9 mAh.g^{-1} at the rates of C/8, C/5, C/2, C and 2C, respectively (Figure 5b).

The formation of the SEI layer and the irreversible capacity is higher for $LiMn_{1.46}Gd_{0.04}Ni_{0.5}O_4$ when compared with $LiMn_{1.5}Ni_{0.5}O_4$ due to its surface area value. Furthermore, the surface area value of this sample is higher than the undoped sample, which affects negatively battery performance.
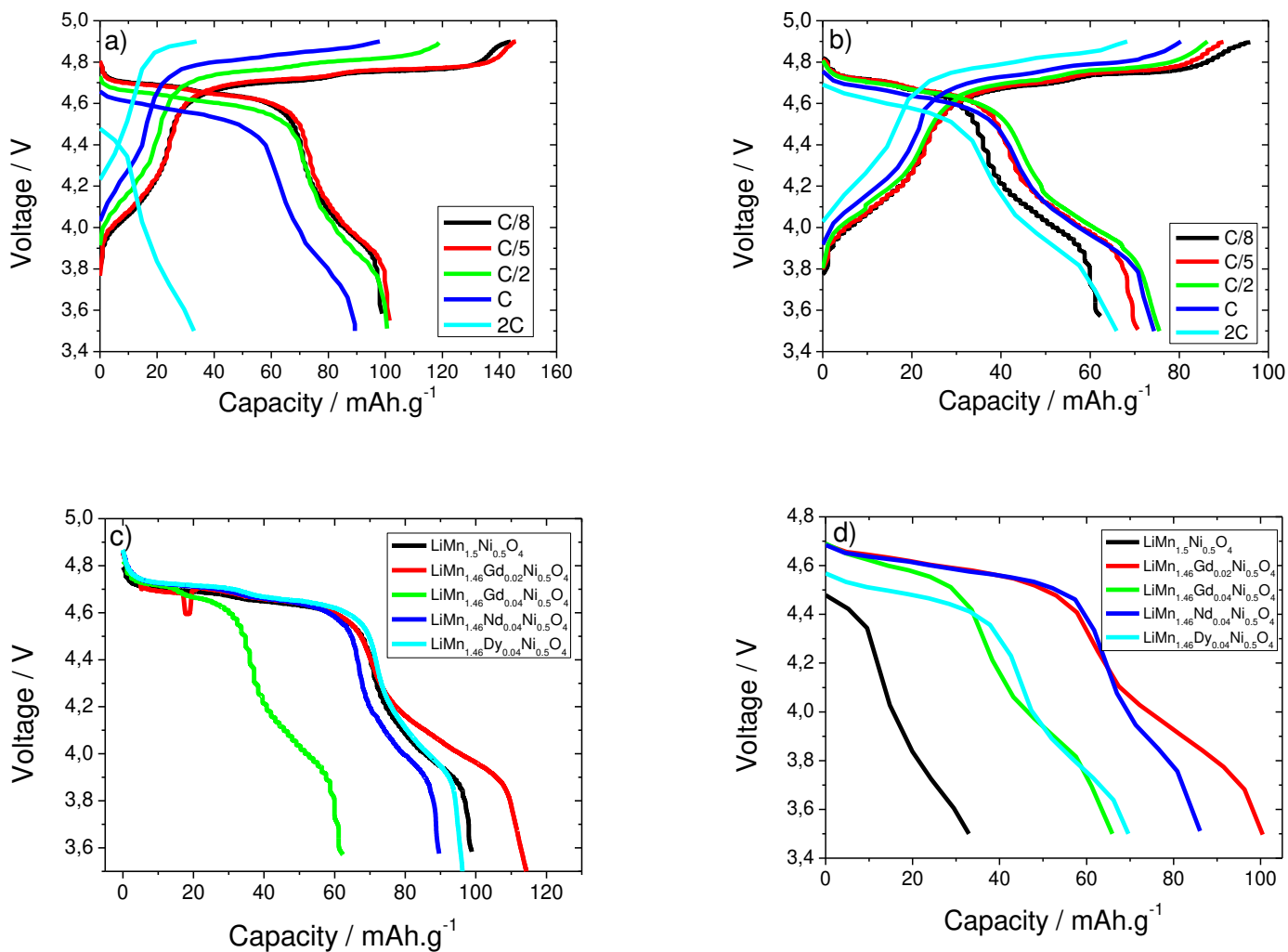
Figure 5 - Charge–discharge curves at C/8 to 2C for the 5th cycle for: $LiMn_{1.5}Ni_{0.5}O_4$ (a) and $LiMn_{1.46}Gd_{0.04}Ni_{0.5}O_4$ (b) cathodes. Charge–discharge curves for all cathodes: at C/8 (c) and 2C (d) for the 5th cycle.

Figure 5 also shows the discharge curves at room temperature for all samples at C/8 (Figure 5c) and 2C (Figure 5d) for the 5th cycle. It is shown that rare earth element doping affects the battery performance of the $LiMn_{1.5}Ni_{0.5}O_4$ cathode material in that depends of its type and amount through of the surface area value. As is observed in the Figures 5c) and d), the voltage plateaus are independent of the doping type and content.

The discharge capacity for the cathodes at C/8 ($LiMn_{1.5}Ni_{0.5}O_4$: 99.3 mAh.g^{-1}; $LiMn_{1.48}Gd_{0.02}Ni_{0.5}O_4$: 113.7 mAh.g^{-1}; $LiMn_{1.46}Gd_{0.04}Ni_{0.5}O_4$: 62.5 mAh.g^{-1}; $LiMn_{1.46}Nd_{0.04}Ni_{0.5}O_4$: 89.5 mAh.g^{-1}; $LiMn_{1.46}Dy_{0.04}Ni_{0.5}O_4$: 96.9 mAh.g^{-1}) are higher than for the cathode material at 2C ($LiMn_{1.5}Ni_{0.5}O_4$: 32.8 mAh.g^{-1}; $LiMn_{1.48}Gd_{0.02}Ni_{0.5}O_4$: 100.3 mAh.g^{-1}; $LiMn_{1.46}Gd_{0.04}Ni_{0.5}O_4$: 65.9 mAh.g^{-1}; $LiMn_{1.46}Nd_{0.04}Ni_{0.5}O_4$: 86.2 mAh.g^{-1}; $LiMn_{1.46}Dy_{0.04}Ni_{0.5}O_4$: 69.2 mAh.g^{-1}) due to electrochemical polarization effect.

It is also observed for the scan rate of 2C, that the 4.7 V discharge voltage plateau decreases and the 4.0 V plateau slowly disappears (Figure 5d).

The spinel cathode doped samples of $LiMn_{1.48}Gd_{0.02}Ni_{0.5}O_4$, $LiMn_{1.46}Nd_{0.04}Ni_{0.5}O_4$ and $LiMn_{1.46}Dy_{0.04}Ni_{0.5}O_4$ demonstrate a higher discharge voltage in comparison with the undoped sample in which the rare earth element doping affects the discharge capacity value of the $LiMn_{1.5}Ni_{0.5}O_4$ cathode material in that the large surface area of the $LiMn_{1.48}Gd_{0.02}Ni_{0.5}O_4$, $LiMn_{1.46}Nd_{0.04}Ni_{0.5}O_4$ and $LiMn_{1.46}Dy_{0.04}Ni_{0.5}O_4$ enhances the electrochemical efficiency through the intercalation and de-intercalation processes of the Li^+ ions.

Further, rare-earth doping tends to stabilize the crystal structure and suppress the Mn dissolution as is the case for $LiMn_{1.46}Nd_{0.04}Ni_{0.5}O_4$ and $LiMn_{1.46}Dy_{0.04}Ni_{0.5}O_4$ samples. Also, if the amount of doping is low, it results in a stable cycling as it is observed for $LiMn_{1.48}Gd_{0.02}Ni_{0.5}O_4$ sample.

Figure 6a) demonstrate the rate performance of the different samples at different C-rates of the discharge value.
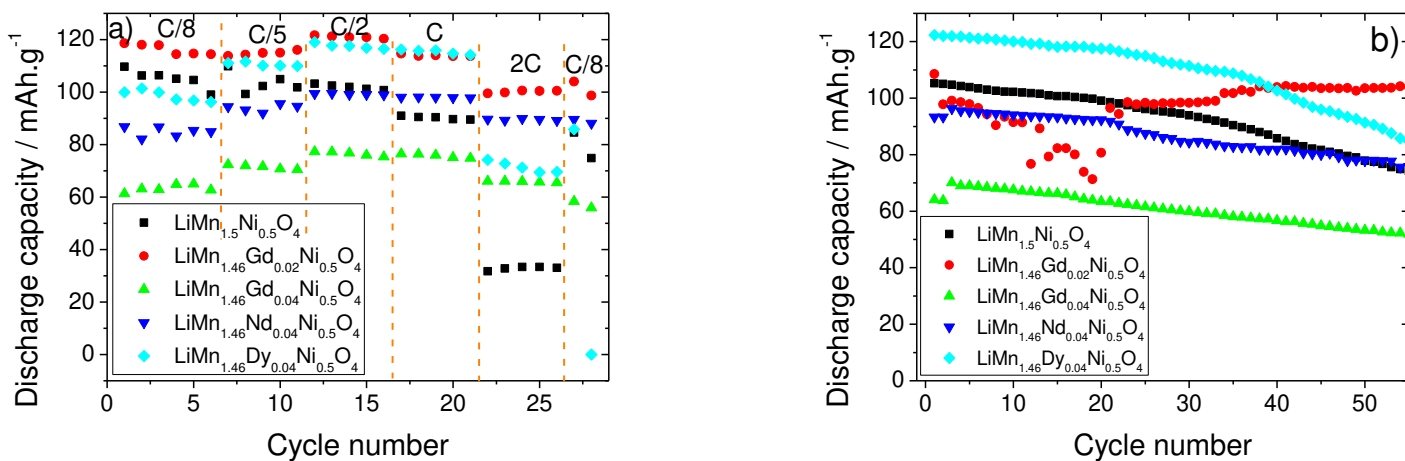
Figure 6 – (a) Rate and (b) cycling performance for the different samples.

Independently of the sample, Figure 6a) shows very stable discharge capacity value for each scan rate as a function of the cycle number, particularly for scan-rates above C/2. Generically, the coulombic efficiency (CE), related to the reversibility of the process, is approximately 90% for all the cathode materials doped with rare earth element.

The $LiMn_{1.48}Gd_{0.02}Ni_{0.5}O_4$ sample shows the best rate performance in comparison with the other samples. Also $LiMn_{1.46}Nd_{0.04}Ni_{0.5}O_4$ and $LiMn_{1.46}Dy_{0.04}Ni_{0.5}O_4$ samples show higher discharge capacity value in comparison with undoped sample for scan-rates above C/5. Moreover, when the current returns to the C/8 rate after cycles at various C-rates, the discharge capacity of all the samples can return to the initial levels, indicating good reversibility. The improved rate performance of rare earth element doping is being attributed to the high surface area value and stabilization of the structure. Rate capability of the cathode material is influenced by several factors as lithium-ion diffusion through the SEI layer, charge transfer reaction and, ohmic polarization, these contributions will be latter discussed through of electrochemical impedance spectroscopy (EIS), Figure 7, and cyclic voltammetry (CV), Figure 8 [45].

The cyclic performances of the all spinel samples at C-rate and room temperature are shown in Figure 6b). It is observed that specific rare earth element doping and amount can improve the cyclic performance of $LiMn_{1.5}Ni_{0.5}O_4$. After 50 cycles, the discharge capacity is 105 mAh.g^{-1}, 84.6 mAh.g^{-1}, 75.7 mAh.g^{-1}, 73.8 mAh.g^{-1} and 51.9 mAh.g^{-1} for $LiMn_{1.48}Gd_{0.02}Ni_{0.5}O_4$, $LiMn_{1.46}Dy_{0.04}Ni_{0.5}O_4$, $LiMn_{1.46}Nd_{0.04}Ni_{0.5}O_4$, $LiMn_{1.5}Ni_{0.5}O_4$ and $LiMn_{1.46}Gd_{0.04}Ni_{0.5}O_4$, respectively, demonstrating that $LiMn_{1.48}Gd_{0.02}Ni_{0.5}O_4$ shows the best cycle stability. Low amount (0.02) of gadolinium (Gd) and neodymium (Nd), and Dysprosium (Dy) improve the cycling stability of the $LiMn_{1.5}Ni_{0.5}O_4$ spinel cathode.

For the initial twenty cycles, it was observed instability of the discharge values for $LiMn_{1.48}Gd_{0.02}Ni_{0.5}O_4$ sample in which is related to the daily fluctuation of the ambient temperature affecting battery temperature. The poor cycling performance of $LiMn_{1.46}Gd_{0.04}Ni_{0.5}O_4$ can be presumably attributed to the surface reactivity of the sample in contact with the liquid electrolyte [46].

Table 4 shows different parameters calculated from the results in Figure 6b) at C-rate based on the charge-discharge curves at room temperature for the different samples.

The initial charge and discharge capacities (Table 4) indicate enhanced capacity for the doped $LiMn_{1.5}Ni_{0.5}O_4$ cathode electrodes, due to the addition of Gd^{3+} and Dy^{3+} in the $LiMn_{1.48}Gd_{0.02}Ni_{0.5}O_4$ and $LiMn_{1.46}Dy_{0.04}Ni_{0.5}O_4$ samples that are affected by the surface area value.

The capacity fade after 55 cycles is 4.15% for $LiMn_{1.48}Gd_{0.02}Ni_{0.5}O_4$ and 19% for $LiMn_{1.46}Ni_{0.5}Nd_{0.04}O_4$ and $LiMn_{1.46}Ni_{0.5}Gd_{0.04}O_4$, in comparison to the value of 29.6% observed for $LiMn_{1.5}Ni_{0.5}O_4$.

Table 4 - Charge and discharge capacities for all samples at C at room temperature.

Capacity and capacity fade	$LiMn_{1.5}Ni_{0.5}O_4$	$LiMn_{1.48}Gd_{0.02}Ni_{0.5}O_4$	$LiMn_{1.46}Ni_{0.5}Gd_{0.04}O_4$	$LiMn_{1.46}Ni_{0.5}Nd_{0.04}O_4$	$LiMn_{1.46}Ni_{0.5}Dy_{0.04}O_4$
First charge capacity (±3) $mAh.g^{-1}$	115.1	139.6	90.5	108.1	128.4
First discharge capacity (±3) $mAh.g^{-1}$	105.3	108.5	64.1	93.3	122.3
2nd and 55th discharge capacity (±3) $mAh.g^{-1}$	105; 74.1	97.8; 104	63.8; 51.9	93.3; 75.8	122.0; 84.7
Initial capacity loss (%)	8.5	22.2	29.2	13.7	4.8
Capacity fade: 55 cycles (%)	29.6	4.15	19.0	19.0	30.7

Also the capacity fade for $LiMn_{1.46}Ni_{0.5}Dy_{0.04}O_4$ is similar to the one observed for the undoped sample. It is observed a higher initial capacity loss for all doped samples except for $LiMn_{1.46}Ni_{0.5}Dy_{0.04}O_4$ in comparison to the undoped sample, indicating that a small fraction of lithium ions is incapable of intercalating back into the host structure due to electrolyte decomposition at high voltage. However, after initial cycling, the cycling efficiency is improved through the formation of protective layer on the electrode surface. Thus, the $LiMn_{1.46}Ni_{0.5}Dy_{0.04}O_4$ (~95%) sample has a higher mean coulombic efficiency than that of the $LiMn_{1.5}Ni_{0.5}O_4$ (~91%) electrode sample.

3.2.2. Electrochemical impedance spectroscopy and CV analysis of the cathodes

EIS measurements were carried out to further understand the effect of rare earth doping into $LiMn_{1.5}Ni_{0.5}O_4$ spinel structure as it was shown that it improves the rate performance and cycling life (Figure 7). Figure 7a) shows the impedance spectra before cycling. Independently of the samples, the impedance spectra of Figure 7a) is characterized by two semicircles in the high-to-medium frequency region followed by a straight line in the low-frequency region. These two semicircles are described by the contributions of three resistances: the ohmic resistance (liquid electrolyte resistance) given by the intercept of the Z_{re} axis at high frequency; the first semicircle, which is ascribed to surface resistance (R_s, solid-electrolyte interface (SEI) layer); and the second semicircle, which is assigned to the charge-transfer resistance process (R_{ct}) [30]. The slope in the low-frequency region represents the Warburg impedance, which is associated with Li^+ diffusion in the bulk material [45]. These semicircles (SC1 and SC2) are identified in the Figure 7a) through an arrow.
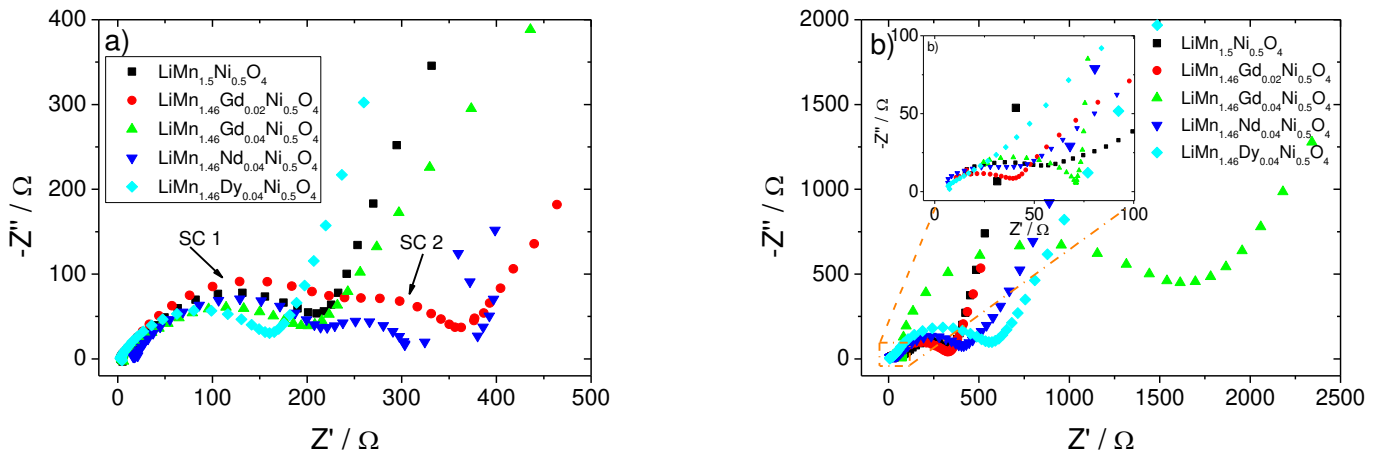

Figure 7 - Electrochemical impedance spectroscopy (EIS) spectra of the different samples: (a) before and (b) after cycling.

The impedance curve shape of after cycling (Figure 7b) is similar to the one before cycling (Figure 7a) in which the rare-earth doping does not affect its shape.

The total resistance value is the sum of the aforementioned resistances and are listed in Table 5 before and after cycling for the different cathodes It is observed that before cycling the lower resistance value is obtained for the $LiMn_{1.46}Ni_{0.5}Dy_{0.04}O_4$ sample, being similar for the rest of the samples.

Table 5 - Total resistance values obtained before and after cycling for all cathode samples.

Sample	Before cycling, R_{total} / Ω	After cycling, R_{total} / Ω
$LiMn_{1.5}Ni_{0.5}O_4$	210	343
$LiMn_{1.48}Gd_{0.02}Ni_{0.5}O_4$	362	337
$LiMn_{1.46}Ni_{0.5}Gd_{0.04}O_4$	203	1685
$LiMn_{1.46}Ni_{0.5}Nd_{0.04}O_4$	340	413
$LiMn_{1.46}Ni_{0.5}Dy_{0.04}O_4$	160	566

After cycling, the total resistance value increases for all samples in comparison with its value before cycling except for the $LiMn_{1.48}Gd_{0.02}Ni_{0.5}O_4$ sample. This increase is due to the SEI formation as it is observed in detail in Figure 7b). It is evident from Figure 7 and Table 5 that $LiMn_{1.48}Gd_{0.02}Ni_{0.5}O_4$ sample presents low resistance value after cycling in comparison to the value before cycling, indicating that this doping suppresses the growth of SEI, which was likely related to the improvement of the cycling stability (Figure 6). The main reason for this fact is the high surface area of this sample and also that small Gd doping reduces Mn dissolution, which results in more stable SEI layer after cycling.

To better understand the polarization effect of the cathodes, the CV curves of the samples, excepting for $LiMn_{1.46}Gd_{0.04}Ni_{0.5}O_4$ sample, are represented in Figure 8. The CV curves are not shown for $LiMn_{1.46}Gd_{0.04}Ni_{0.5}O_4$ due the poor battery performance and high resistance value (Figure 6). Figure 8a shows the CV curves of the $LiMn_{1.48}Gd_{0.02}Ni_{0.5}O_4$ sample for the first three cycles. Independently of the cycle number, it is observed that the corresponding area for each peak is very similar, showing a low electrochemical polarization.
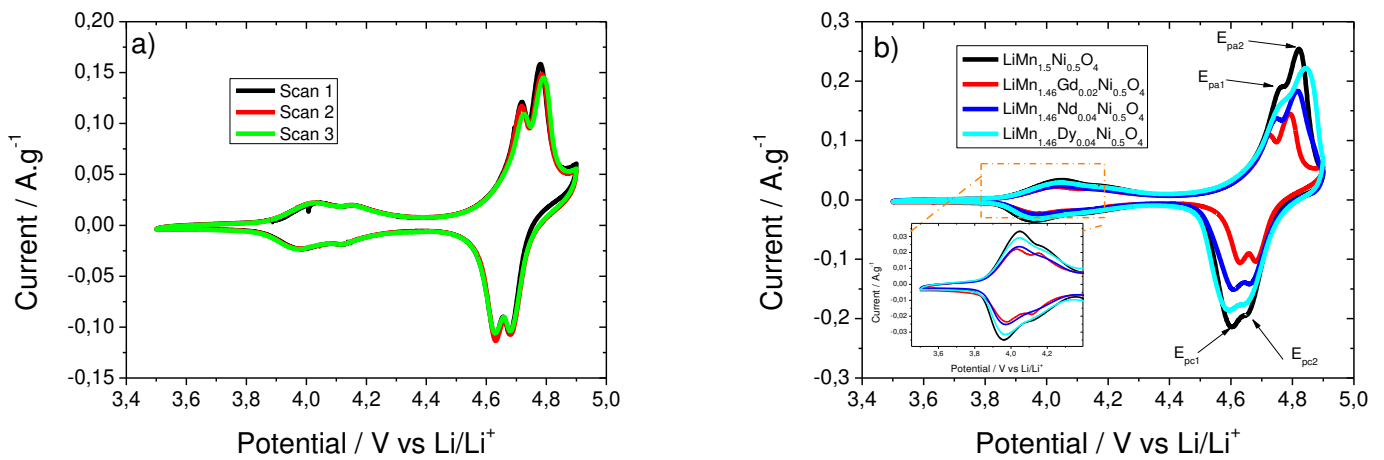

Figure 8- CV curves for the: a) $LiMn_{1.48}Gd_{0.02}Ni_{0.5}O_4$ sample as a function of the scan number and for all samples at the 3th scan except for $LiMn_{1.46}Gd_{0.04}Ni_{0.5}O_4$ sample.

Figure 8a) shows also a typical CV profile with one weak pair of redox peaks at around 4.0 V (Mn^{3+}/Mn^{4+}) and two pairs of well separated strong redox peaks at 4.6 - 4.7 V indicating a two-stage (Ni^{2+}/Ni^{3+} and Ni^{3+}/Ni^{4+}) Li^+ extraction (insertion) from(into) the spinel framework [19]. These redox peaks are also observed for the other samples as it is shown in Figure 8b).

The intensity of the peaks of Figure 8b) for all doped samples decreases in comparison with the undoped sample.

The main characteristics of the CV results for the two pair of redox peaks between 4.6 V and 4.7 V are summarized in table 6. The symbols are defined as follows: E_{pa}: anodic peak potential, E_{pc}: cathodic peak potential. The numbers 1 and 2 denote the redox couple at lower and higher potential, respectively.

Taking into account the results in table 6, it is observed that ΔE_{p1} and ΔE_{p2} are higher than the ideal condition ($\Delta E_p = 0$) which indicates that $Ni^{2+} \leftrightarrow Ni^{4+}$ is controlled by insertion/disinsertion of Li^+ in the cathode electrodes regardless of the sample.

Table 6 - Electrochemical parameters from CV.

Sample	Potential values / V					
	E_{pa1}	E_{pa2}	E_{pc1}	E_{pc2}	ΔE_{p1}	ΔE_{p2}
$LiMn_{1.5}Ni_{0.5}O_4$	4.76	4.82	4.60	4.66	0.16	0.16
$LiMn_{1.48}Ni_{0.5}Gd_{0.02}O_4$	4.73	4.79	4.62	4.68	0.11	0.11
$LiMn_{1.46}Ni_{0.5}Nd_{0.04}O_4$	4.75	4.82	4.61	4.66	0.14	0.16
$LiMn_{1.46}Ni_{0.5}Dy_{0.04}O_4$	4.76	4.84	4.59	4.65	0.17	0.19

The lower values of ΔE_{p1} and ΔE_{p2} for the $LiMn_{1.48}Ni_{0.5}Gd_{0.02}O_4$ sample in comparison with the undoped sample is due to the higher surface area value in which the lithium diffusion behavior is enhanced.

Through table 6, the potential difference follows the order $LiMn_{1.48}Ni_{0.5}Gd_{0.02}O_4$ < $LiMn_{1.46}Ni_{0.5}Gd_{0.04}O_4$ ≈ $LiMn_{1.5}Ni_{0.5}O_4$ < $LiMn_{1.46}Ni_{0.5}Dy_{0.04}O_4$, indicating that the $LiMn_{1.48}Ni_{0.5}Gd_{0.02}O_4$ sample has the lowest electrochemical polarization, reflecting its

increased conductivity and reactivity for extraction-reinsertion of lithium-ions in the active material.

3.2.3. Comparison of the LiMn$_{1.5}$Ni$_{0.5}$O$_4$ spinel cathode produced in this work with the literature

It is very useful to compare the electrochemical performance of the samples with related dopings reported in the literature for LiMn$_{1.5}$Ni$_{0.5}$O$_4$ based cathodes once this is the first time the spinel cathode structure is doped with rare earth elements.

Though the powder size and the composition of the cathode electrodes reported in table 7 are not the same for all samples, it is observed that the rare earth doping improves the cyclability of the LiMn$_{1.5}$Ni$_{0.5}$O$_4$ spinel cathode at room temperature.

Table 7 - Comparison of the discharge capacity value for the rare-earth doped LiMn$_{1.5}$Ni$_{0.5}$O$_4$ and doping with different atoms reported in the literature.

Cathode	Element doping	Size / μm	Discharge capacity / mAh.g^{-1}	Ref
LiNi$_{0.45}$Al$_{0.10}$Mn$_{1.45}$O$_4$	Al	~ 0.6	127 at C	[47]
LiNi$_{0.5}$Co$_{0.05}$Mn$_{1.45}$O$_4$	Co	3	118 at 5C	[48]
LiMn$_{1.4}$Cr$_{0.2}$Ni$_{0.4}$O$_4$	Cr	< 1	130.8 at 0.15C	[49]
LiNi$_{0.45}$Cu$_{0.05}$Mn$_{1.5}$O$_4$	Cu	-----	124.5 at 5C	[50]
LiNi$_{0.5}$Mn$_{1.5}$O$_{3.975}$F$_{0.05}$	F	-----	142 at 0.25C	[51]
LiMn$_{1.5}$Ni$_{0.42}$Fe$_{0.08}$O$_4$	Fe	~ 1	136 at C/6	[45]
LiMn$_{1.5}$Ni$_{0.42}$Ga$_{0.08}$O$_4$	Ga		~ 128 at C/6	[30]
LiMg$_{0.05}$Ni$_{0.45}$Mn$_{1.5}$O$_4$	Mg	0.02 – 0.08	117 at C	[31]
LiMn$_{1.4}$Ni$_{0.55}$Mo$_{0.05}$O$_4$	Mo	3-5	122.7 at 0.1C	[32]
LiNi$_{0.525}$Mn$_{1.425}$Nb$_{0.05}$O$_4$	Nb	1-2	102.7 at C	[33]
LiNi$_{0.48}$Rh$_{0.02}$Mn$_{1.5}$O$_4$	Rh	0.08	92.4 at C	[34]
LiNi$_{0.4}$Ru$_{0.05}$Mn$_{1.5}$O$_4$	Ru	0.6 - 1	133.4 at 1C	[52]
LiNi$_{0.5}$Mn$_{1.5}$O$_{3.95}$S$_{0.05}$	S	0.01	116 at 0.2C	[39]
LiNi$_{0.5}$Sm$_{0.01}$Mn$_{1.49}$O$_4$	Sm	0.3 - 0.5	125 at C	[36]
LiNi$_{0.5}$Mn$_{1.0}$Ti$_{0.5}$O$_4$	Ti	< 1	206.5	[37]
LiNi$_{0.4}$Ti$_{0.1}$Mn$_{1.5}$O$_4$	Ti	0.3 - 3.0	134.8 at C	[53]
Li$_{0.995}$V$_{0.005}$Ni$_{0.5}$Mn$_{1.5}$O$_4$	V	0.1 - 0.2	130 at 0.8C	[38]
LiW$_{0.005}$Ni$_{0.5}$Mn$_{1.495}$O$_4$	W	0.5	124.9 at 0.1C	[41]
LiZn$_{0.08}$Ni$_{0.42}$Mn$_{1.5}$O$_4$	Zn	-----	118 at 0.5C	[40]
LiMn$_{1.48}$Ni$_{0.5}$Gd$_{0.02}$O$_4$	Gd	0.05-0.2	104 at C	This work

Due to their unusual physical and chemical properties and also to the fact that the rare earth elements presented in this work are more abundant on average in the Earth's crust than silver, gold, or platinum, and taking into account their improvement in battery performance, the rare earth doping of $LiMn_{1.5}Ni_{0.5}O_4$ is an excellent alternative to conventional doping for this spinel structure to solve the problem of capacity fade as it is shown in table 7.

Conclusion

$LiMn_{1.5}Ni_{0.5}O_4$ with spinel type of structure was synthesized by sol–gel method and doped with different rare earth elements. The rare-earth elements used in this work are neodymium (Nd), gadolinium (Gd) and dysprosium (Dy) with concentrations of 0.02 and 0.04 for Gd and 0.04 for the other elements. The particle size of all samples are approximately between 50 nm to 200 nm in that the doping by rare earth elements increases the surface area of $LiMn_{1.48}Gd_{0.02}Ni_{0.5}O_4$ which can be related with the specific distribution of the agglomerated nanoparticles. The rare earth doping does not affect the formation of a cubic spinel structure. The charge–discharge curves show significant high discharge capability values at room temperature with rare earth doping, depending on the amount and type of the rare earth. After 55 cycles at C, the discharge capacity values are 104 $mAh.g^{-1}$, 84.7 $mAh.g^{-1}$, 75.8 $mAh.g^{-1}$, 74.1 $mAh.g^{-1}$ and 51.9 $mAh.g^{-1}$ for $LiMn_{1.48}Ni_{0.5}Gd_{0.02}O_4$, $LiMn_{1.46}Ni_{0.5}Dy_{0.04}O_4$, $LiMn_{1.46}Ni_{0.5}Nd_{0.04}O_4$, $LiMn_{1.5}Ni_{0.5}O_4$ and $LiMn_{1.46}Ni_{0.5}Gd_{0.04}O_4$. Further, the rare earth doping affects the overall electrical conductivity of the cathode electrode. The rare earth doping with Gd and Dy exhibit better electrochemical cycling performance in comparison to pristine $LiMn_{1.5}Ni_{0.5}O_4$.

In summary, $LiMn_{1.48}Ni_{0.5}Gd_{0.02}O_4$ is an excellent active material for cathodes in rechargeable lithium-ion battery applications and for high scan-rate (C). This sample also shows best electrochemical performance compared with related materials presented in the literature.

Acknowledgments

References

[1] A. Sternberg, A. Bardow, Energy & Environmental Science, 8 (2015) 389-400.

[2] F. O Rourke, F. Boyle, A. Reynolds, Applied Energy, 87 (2010) 398-409.

[3] L. Lu, X. Han, J. Li, J. Hua, M. Ouyang, Journal of Power Sources, 226 (2013) 272-288.

[4] M.M. Thackeray, C. Wolverton, E.D. Isaacs, Energy & Environmental Science, 5 (2012) 7854-7863.

[5] H. Chen, T.N. Cong, W. Yang, C. Tan, Y. Li, Y. Ding, Progress in Natural Science, 19 (2009) 291-312.

[6] J.B. Goodenough, K.-S. Park, Journal of the American Chemical Society, 135 (2013) 1167-1176.

[7] D.L. Wood Iii, J. Li, C. Daniel, Journal of Power Sources, 275 (2015) 234-242.

[8] M. Park, X. Zhang, M. Chung, G.B. Less, A.M. Sastry, Journal of Power Sources, 195 (2010) 7904-7929.

[9] C.M. Costa, M.M. Silva, S. Lanceros-Mendez, RSC Advances, 3 (2013) 11404-11417.

[10] A. Gören, C.M. Costa, M.M. Silva, S. Lanceros-Méndez, Composites Part B: Engineering, 83 (2015) 333-345.

[11] E. Antolini, Solid State Ionics, 170 (2004) 159-171.

[12] A.R. Armstrong, A.J. Paterson, A.D. Robertson, P.G. Bruce, Chemistry of Materials, 14 (2002) 710-719.

[13] W. Yuan, J. Yan, Z. Tang, O. Sha, J. Wang, W. Mao, L. Ma, Journal of Power Sources, 201 (2012) 301-306.

[14] A. Manthiram, K. Chemelewski, E.-S. Lee, Energy & Environmental Science, 7 (2014) 1339-1350.

[15] C.A.J. Fisher, V.M. Hart Prieto, M.S. Islam, Chemistry of Materials, 20 (2008) 5907-5915.

[16] P. Ram, A. Goren, S. Ferdov, M.M. Silva, R. Singhal, C.M. Costa, R.K. Sharma, S. Lanceros-Mendez, New Journal of Chemistry, 40 (2016) 6244-6252.

[17] M. Wohlfahrt-Mehrens, C. Vogler, J. Garche, Journal of Power Sources, 127 (2004) 58-64.

[18] R.J. Gummow, A. de Kock, M.M. Thackeray, Solid State Ionics, 69 (1994) 59-67.

[19] G.B. Zhong, Y.Y. Wang, Z.C. Zhang, C.H. Chen, Electrochimica Acta, 56 (2011) 6554-6561.

[20] T.-F. Yi, J. Mei, Y.-R. Zhu, Journal of Power Sources, 316 (2016) 85-105.

[21] C.J. Jafta, M.K. Mathe, N. Manyala, W.D. Roos, K.I. Ozoemena, ACS Applied Materials & Interfaces, 5 (2013) 7592-7598.

[22] X. Zhang, F. Cheng, K. Zhang, Y. Liang, S. Yang, J. Liang, J. Chen, RSC Advances, 2 (2012) 5669-5675.

[23] R. Santhanam, B. Rambabu, Journal of Power Sources, 195 (2010) 5442-5451.

[24] C. Julien, A. Mauger, K. Zaghib, H. Groult, Inorganics, 2 (2014) 132.

[25] M.-W. Jang, H.-G. Jung, B. Scrosati, Y.-K. Sun, Journal of Power Sources, 220 (2012) 354-359.

[26] S.B. Park, W.S. Eom, W.I. Cho, H. Jang, Journal of Power Sources, 159 (2006) 679-684.

[27] A. Milewska, Ł. Kondracki, M. Molenda, M. Bakierska, J. Molenda, Solid State Ionics, 267 (2014) 27-31.

[28] S.-W. Oh, S.-H. Park, J.-H. Kim, Y.C. Bae, Y.-K. Sun, Journal of Power Sources, 157 (2006) 464-470.

[29] R. Alcántara, M. Jaraba, P. Lavela, J.M. Lloris, C. Pérez Vicente, J.L. Tirado, Journal of The Electrochemical Society, 152 (2005) A13-A18.

[30] D.W. Shin, A. Manthiram, Electrochemistry Communications, 13 (2011) 1213-1216.

[31] U. Lafont, C. Locati, W.J.H. Borghols, A. Łasińska, J. Dygas, A.V. Chadwick, E.M. Kelder, Journal of Power Sources, 189 (2009) 179-184.

[32] T.-F. Yi, B. Chen, Y.-R. Zhu, X.-Y. Li, R.-S. Zhu, Journal of Power Sources, 247 (2014) 778-785.

[33] T.-F. Yi, Y. Xie, Y.-R. Zhu, R.-S. Zhu, M.-F. Ye, Journal of Power Sources, 211 (2012) 59-65.

[34] P. Wu, X.L. Zeng, C. Zhou, G.F. Gu, D.G. Tong, Materials Chemistry and Physics, 138 (2013) 716-723.

[35] H. Wang, T.A. Tan, P. Yang, M.O. Lai, L. Lu, The Journal of Physical Chemistry C, 115 (2011) 6102-6110.

[36] M. Mo, K.S. Hui, X. Hong, J. Guo, C. Ye, A. Li, N. Hu, Z. Huang, J. Jiang, J. Liang, H. Chen, Applied Surface Science, 290 (2014) 412-418.

[37] M. Lin, S.H. Wang, Z.L. Gong, X.K. Huang, Y. Yang, Journal of The Electrochemical Society, 160 (2013) A3036-A3040.

[38] M.C. Kim, K.-W. Nam, E. Hu, X.-Q. Yang, H. Kim, K. Kang, V. Aravindan, W.-S. Kim, Y.-S. Lee, ChemSusChem, 7 (2014) 829-834.

[39] Y.-K. Sun, S.W. Oh, C.S. Yoon, H.J. Bang, J. Prakash, Journal of Power Sources, 161 (2006) 19-26.

[40] Z. Yang, Y. Jiang, J.-H. Kim, Y. Wu, G.-L. Li, Y.-H. Huang, Electrochimica Acta, 117 (2014) 76-83.

[41] S.J.R. Prabakar, S.C. Han, S.P. Singh, D.K. Lee, K.-S. Sohn, M. Pyo, Journal of Power Sources, 209 (2012) 57-64.

[42] S. Balaji, T.M. Chandran, D. Mutharasu, Ionics, 18 (2012) 549-558.

[43] J. Mao, K. Dai, M. Xuan, G. Shao, R. Qiao, W. Yang, V.S. Battaglia, G. Liu, ACS Applied Materials & Interfaces, 8 (2016) 9116-9124.

[44] J. Li, L. Baggetto, S.K. Martha, G.M. Veith, J. Nanda, C. Liang, N.J. Dudney, Advanced Energy Materials, 3 (2013) 1275-1278.

[45] J. Liu, A. Manthiram, The Journal of Physical Chemistry C, 113 (2009) 15073-15079.

[46] Q. Wu, X. Zhang, S. Sun, N. Wan, D. Pan, Y. Bai, H. Zhu, Y.-S. Hu, S. Dai, Nanoscale, 7 (2015) 15609-15617.

[47] G.B. Zhong, Y.Y. Wang, X.J. Zhao, Q.S. Wang, Y. Yu, C.H. Chen, Journal of Power Sources, 216 (2012) 368-375.

[48] S.W. Oh, S.-T. Myung, H.B. Kang, Y.-K. Sun, Journal of Power Sources, 189 (2009) 752-756.

[49] T.-F. Yi, J. Shu, Y.-R. Zhu, R.-S. Zhu, Journal of Physics and Chemistry of Solids, 70 (2009) 153-158.

[50] O. Sha, Z. Qiao, S. Wang, Z. Tang, H. Wang, X. Zhang, Q. Xu, Materials Research Bulletin, 48 (2013) 1606-1611.

[51] X.X. Xu, J. Yang, Y.Q. Wang, Y.N. NuLi, J.L. Wang, Journal of Power Sources, 174 (2007) 1113-1116.

[52] J.S. Chae, M.R. Jo, Y.-I. Kim, D.-W. Han, S.-M. Park, Y.-M. Kang, K.C. Roh, Journal of Industrial and Engineering Chemistry, 21 (2015) 731-735.

[53] Y.-Z. Jin, Y.-Z. Lv, Y. Xue, J. Wu, X.-G. Zhang, Z.-B. Wang, RSC Advances, 4 (2014) 57041-57047.